Nanoscale

COMMUNICATION

View Article Online
View Journal | View Issue



Cite this: *Nanoscale*, 2026, **18**, 10021

Received 22nd February 2026,
Accepted 6th April 2026

DOI: 10.1039/d6nr00739b

rsc.li/nanoscale

# Continuous flow synthesis of MOF/nanocarbon composites

Almond Lau, [a] Ji Feng, *[a] Stefan H. Bossmann,[b,c] Dymphna Sebastian,[b,c] Christopher M. Sorensen[b,d] and Igor V. Novosselov *[a]

**Zirconium-based metal–organic frameworks (Zr-MOFs), such as UiO-66-$NH_2$, exhibit high surface areas and chemical stability, while graphene provides unique electrical properties and high mechanical strength. Hence, nanocomposites that integrate graphene into Zr-MOFs can enhance interfacial charge transfer and offer new functionalities for porous materials. However, controlled and cost-effective synthesis of high-quality Zr-MOF/graphene nanocomposites has not been demonstrated. Here, we report a supercritical $CO_2$ ($scCO_2$)-assisted continuous-flow process for depositing nanometer-scale UiO-66-$NH_2$ layers on reactive, carboxylic-modified graphene aggregates (CGA). This approach is enabled by rapid nucleation and growth of UiO-66-$NH_2$ (~1 min) and yields 3.5 g $h^{-1}$ of MOF/CGA nanocomposites in a lab-scale 150 cc reactor. CGA, produced by a chamber-explosion method followed by surface modification to add carboxylic acid groups, was continuously mixed with Zr-MOF precursors in a $scCO_2$ reactor, resulting in a MOF/CGA composite with near-uniform 10–20 nm-thick MOF coating. The influence of graphene loading (5–30 wt%) on the structural, physical, electrical, and chemical properties of the composites was examined. The resulting materials exhibit intimate contact between MOF and graphene layers, high BET surface areas, and enhanced photothermal responses under solar illumination, highlighting their potential for photocatalysis and other applications.**

## Introduction

Metal–organic framework (MOF)-graphene-based composites have emerged as a versatile class of hybrid materials that integrate the high surface area, tunable porosity, and chemical functionality of MOFs with the excellent electrical conductivity, mechanical robustness, and light-absorption properties of graphene.[1–3] These composites have shown a potential for a broad range of applications, such as chemical sensing, adsorption and separation, energy storage, and environmental remediation.[4–9] In particular, MOF-graphene composites have emerged as promising platforms for catalytic and photocatalytic reactions, in which MOFs provide active sites for molecular adsorption and transformation, while graphene enhances charge transport and light utilization. Incorporating graphene often results in smaller MOF crystals and altered crystal growth orientation, thus increasing the density of accessible active sites.[10,11]

Despite these advantages, the practical deployment of MOF-graphene-based composites remains limited due to challenges of scalable synthesis. Most reported methods rely on batch processes, which suffer from poor control over composite morphology, long synthesis time (>24 h), limited throughput, and difficulty in achieving uniform MOF-graphene interfacial contact.[12,13] Typically, MOF/graphene composites are synthesized by hydro-/solvothermal methods, in which the graphene material is simply added to the dissolved MOF precursors before heating. Other methods include seeded growth, layer-by-layer deposition, mechanochemical, direct mixing, and pickering emulsion.[14–17] To date, continuous-flow synthesis of MOF-graphene composites remains unexplored, and no reports have demonstrated scalable production routes that address material quality, interfacial control, or quantified manufacturing throughput.

Several factors have hindered the large-scale production of MOF-graphene-based composites. First, graphene itself remains challenging to manufacture at scale. Common exfoliation approaches relying on concentrated acids and intensive shear forces involve hazardous chemicals and high energy consumption. Second, the scalable synthesis of MOFs is nontrivial, particularly for frameworks containing secondary building units with slow formation kinetics.[18–20] In addition,

[a]*Department of Mechanical Engineering and Institute for Nano-Engineered Systems, University of Washington, 3900 E Stevens Way NE, Seattle, WA 98195, USA. E-mail: jfeng003@uw.edu, ivn@uw.edu*
[b]*HydroGraph Clean Power, Inc, 809H Levee Drive, Manhattan, KS 66502, USA*
[c]*Department of Cancer Biology, University of Kansas Medical School, Kansas City, KS 66160, USA*
[d]*Department of Physics, Kansas State University, Manhattan, KS 66506, USA*

surface modification of graphene to promote MOF nucleation and growth is challenging.[21] Graphene needs to be oxidized to introduce surface functional groups, such as carboxyl (–COOH) moieties. These groups can coordinate with metal ions or interact with MOF organic linkers to initiate heterogeneous MOF nucleation.[22,23] However, excessive oxidation reduces graphene's electrical conductivity, thereby compromising the functional performance of the resulting composites; *e.g.*, to induce a photocatalytic effect, graphene-based composites require intimate interfacial contact to enable charge transfer.[24]

Here, we present a scalable approach that integrates graphene-based nanomaterial production followed by controlled growth of MOF nanoscale layers. The graphene was synthesized using a novel chamber-explosion method that produces high-quality, multilayer graphene.[25–27] This patented method has been scaled up to production levels.[28] We have previously reported a supercritical $CO_2$ ($scCO_2$)-assisted continuous synthesis of MOFs.[29,30] $ScCO_2$ is a green solvent with a relatively low critical temperature (31.1 °C) and pressure (7.4 MPa). It is particularly well-suited for the processing of heat-sensitive materials. We have established the role of $scCO_2$ in accelerating the MOF nucleation and growth, using HKUST-1 as an example, and achieved high-quality MOF production in ~10 seconds.[31]

This work presents a novel approach to rapidly produce MOF/graphene composites by combining large-scale chamber explosion graphene synthesis and continuous-flow MOF synthesis. $ScCO_2$ enables effective MOF anchoring, leading to high-yield, scalable synthesis of UiO-66-$NH_2$/graphene nanocomposites. The resulting composites consist of uniform MOF shells that conformally coat fractal graphene aggregates, leading to intimate interfacial contact, increased MOF structural defects, and higher BET surface areas. The novel MOF/graphene materials exhibit strong photothermal responses under solar illumination and are promising candidates for photocatalytic applications.

# Experimental

### Material synthesis

Graphene materials were produced by HydroGraph Clean Power, Inc. Their patented method[28] uses a chamber explosion synthesis process,[26,32] which involves igniting mixtures of acetylene and oxygen with an atomic ratio of O/C = 0.3 in a closed chamber. The result is fractal aggregates with radii of gyration of ~120 nm, composed of monomers 20–50 nm in lateral extent, with an average of 6–7 turbostratic graphene layers. This product, named FGA-1, was subsequently modified to form a carboxyl-modified graphene aggregate (CGA), as detailed in the SI.

Synthesis of UiO-66-$NH_2$, U66N/CGA5, U66N/CGA10, U66N/CGA20, and U66N/CGA30 was conducted in a supercritical $CO_2$ ($scCO_2$) continuous flow reactor (Fig. 1a and Fig. S1). The numbers (5, 10, 20, and 30) represent the % mass of CGA in the sample. During synthesis, $CO_2$ supplied from a gas cylinder is cooled to the liquid phase at ~0 °C and pumped at 20 mL $min^{-1}$ into a coiled heater, where it is heated to 180 °C before being injected into a mixing section. The precursor solution is injected into the mixing section at 20 mL $min^{-1}$, and the mixture then flows into the reactor (ID = 0.957-inch tubing). A wrapped tape heater maintains the fluid at 140 °C. After exiting the reactor, the fluid is cooled and passed through the back-pressure regulator (BPR) set to 10 MPa before it is collected at ambient temperature and pressure in a bottle, while the $CO_2$ naturally separates and is vented. The total residence time of the fluid mixture in the heated reactor sections is ~1.2 min (see SI). The precursor formulation and material activation are detailed in the SI.

### Material characterization

The crystallinity and material structures were characterized by powder X-ray diffraction (PXRD, Bruker D8 Discover) using a microfocus X-ray source and Pilatus 100 K large-area 2D detector, operating at 50 kV and 1000 μA over an angular range of $2\theta$ = 5–45° in increments of 5.5°. Particle morphology was analyzed by scanning electron microscopy (SEM; FEI Sirion XL30) at 5 kV. Samples were prepared for SEM by depositing and drying a drop of the ethanol-dispersed sample onto an oxygen-plasma-cleaned silicon wafer. The sample was coated with ~5 nm of platinum using a Leica EM ACE600 sputter coater. For more detailed morphological analysis, the samples were also imaged by transmission electron microscopy (TEM; FEI Tecnai G2 F20 SuperTwin) at 200 kV. The BET surface area was determined using nitrogen sorption at 77 K with a Micromeritics 3Flex gas sorption analysis system. The samples were heated at 140 °C for 12 h using a Micromeritics Smart VacPrep to remove any adsorbed molecules before analysis. Raman spectra were collected at 532 nm on a Renishaw InVia Raman microscope at 0.5% power density, with a wavenumber range of 1000–2200 $cm^{-1}$. Thermal stability data were collected *via* thermogravimetric analysis (TGA, Mettler Toledo TGA/DSC 3+) on ~4 mg of powder sample to obtain mass loss curves as a function of temperature by 10 °C $min^{-1}$ from room temperature to 1000 °C. UV-vis diffuse reflectance spectra were collected using a Cary 5000 UV-Vis-NIR spectrophotometer (Agilent) operated in diffuse and specular reflection (DSR) mode. $BaSO_4$ was used as the reflectance reference and as a diluent for sample preparation. All powder samples were diluted with $BaSO_4$ at a mass ratio of 1 : 200 to ensure sufficient diffuse conditions. The measured reflectance spectra were normalized by the $BaSO_4$ reference spectrum and converted to the Kubelka–Munk function for optical analysis. Photothermal measurements were conducted using a solar lamp (0.1 W $cm^{-2}$) and an infrared (IR) camera (Kaiweets KTI-W01) with emissivity set to 0.95. The UiO-66-$NH_2$ and U66N/CGA samples were dispersed to 0.5 mg $mL^{-1}$ in water, and 350 μL of each solution was placed in a 96-well optical reaction plate. The sample plate was placed under the lamp and imaged at 15 min intervals.

 

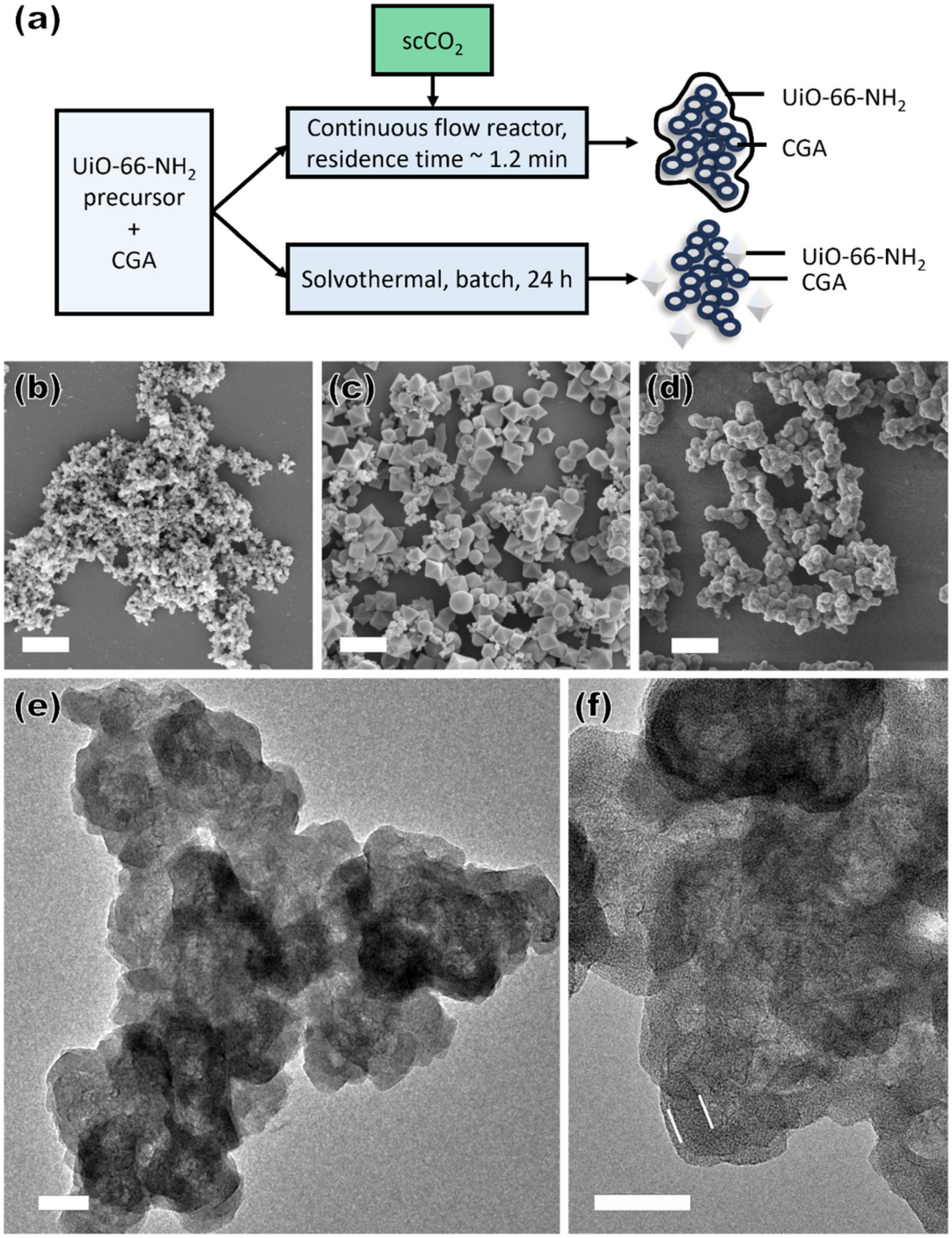


**Fig. 1** (a) Schematic illustration of the synthesis and the resulting products. Morphological analysis: SEM images (b) CGA, (c) U66N/CGA nanocomposites synthesized without $scCO_2$, and (d) U66N/CGA20 synthesized with $scCO_2$. TEM images of U66N/CGA30 synthesized with $scCO_2$ are shown in (e) and (f). The scale bars are 500 nm in (b–d) and 50 nm in (e) and (f). The white lines in (f) indicate the UiO-66-$NH_2$ shell.

## Results

The $scCO_2$-assisted continuous-flow process yielded ~3.5 g $h^{-1}$ in a lab-scale reactor. The resulting products consist of UiO-66-$NH_2$-coated CGA, unlike in the solvothermal synthesis methods (Fig. 1a). The SEM and TEM images of CGA (Fig. 1b and Fig. S2) confirmed its fractal morphology: rather than extended planar sheets, the material comprises aggregated graphene domains, each consisting of interconnected monomers with sizes ranging from 30 to 50 nm. Fig. 1c illustrates the U66N/CGA product synthesized without $scCO_2$ at 140 °C in a DMF solution containing 0.05 M $ZrOCl_2$, with acetic acid

added as a modulator for MOF crystallization. Although the CGA was carboxylated, it did not lead to MOF nucleation on its surface or coating; instead, the product consists of both UiO-66-$NH_2$ octahedral particles and free CGA. In contrast, when CGA is processed with $scCO_2$, the U66N/CGA composites exhibit no discrete crystals. The CGA morphology remains unchanged within the composite structure (Fig. 1d and Fig. S6). Notably, no free or uncoated graphene domains are observed, indicating that UiO-66-$NH_2$ fully encapsulates the CGA during the synthesis. TEM analysis (Fig. 1e) reveals MOF-coated aggregated graphene clusters with sizes on the order of a few hundred nanometers. A decrease in shell thickness is observed with increasing CGA content. The MOF coating is ~40 nm thick for the U66N/CGA10 composite (Fig. S7), whereas the shell thins to 16 ± 3 nm in the U66N/CGA30 sample (Fig. 1f). This decrease in shell thickness indicates that higher CGA content spreads the available MOF precursors over its larger surface area, thereby leading to the formation of thinner yet continuous UiO-66-$NH_2$ shells. For the lowest CGA case, U66N/CGA5 shows structural inhomogeneity, likely due to the low CGA content, which favours a fraction of the MOF to form independent crystals rather than MOF/CGA composites (Fig. S8).

Structural analysis confirms the formation of crystalline UiO-66-$NH_2$ for all CGA loadings. The XRD pattern (Fig. 2a) of CGA exhibits a characteristic broad peak at $2\theta \approx 25.4°$, consistent with the (002) plane reflection typically observed in reduced graphene oxide. All $scCO_2$-assisted continuous-flow synthesized composites display the well-defined diffraction peaks of UiO-66-$NH_2$, including the reflections at approximately 7.3° and 8.4°, corresponding to the (111) and (200) planes. The slight increase in intensity at approximately $2\theta \approx 25°$ in the composite samples further indicates the incorporation of CGA into the UiO-66-$NH_2$ framework. BET shows that the surface areas of UiO-66-$NH_2$, U66N/CGA5, U66N/CGA10, U66N/CGA20, and U66N/CGA30 are 978, 1011, 931, 859, and 795 $m^2\ g^{-1}$, respectively (Fig. 2b). Although CGA itself does not exhibit a high surface area (140 $m^2\ g^{-1}$, Fig. S3), the elevated values of the composites can be attributed to defect formation. The structure of the UiO-66-$NH_2$ coating is consistent with that of the neat MOF. With up to 20 wt% of CGA, the MOF/CGA exhibits high-quality UiO-66-$NH_2$, as evidenced by the BET surface area and pore sizes.

Raman spectra (Fig. 2c) show the D and G bands of CGA at 1341 and 1588 $cm^{-1}$, respectively. The persistence of the D band after MOF coating suggests that no significant reduction or oxidation of CGA occurs during the coating process. Notably, the G band shifts to higher wavenumbers, indicative of electron transfer from CGA to UiO-66-$NH_2$, which is consistent with strong interfacial coupling in the composite structure.[33–35] The intensity ratio of the D and G bands can be used to evaluate the disorder level in graphene-based structures; however, the overlap of these bands with the vibrational features of UiO-66-$NH_2$ does not allow for a quantitative analysis of the composite samples.

Defect level and thermal stability were evaluated by TGA analysis (Fig. 3). For UiO-66-$NH_2$, the mass loss below 150 °C corresponds to the evaporation of adsorbed moisture, while a distinct feature around 280 °C is attributed to the removal of the acetic acid modulator. The BDC-$NH_2$ linker begins to decompose at ~320 °C, peaking at 440 °C. When normalized by the final $ZrO_2$ residue, UiO-66-$NH_2$ exhibits a weight percentage of 228% at 320 °C. A defect-free UiO-66-$NH_2$ with the ideal $Zr_6O_6$ $(BDC\text{-}NH_2)_6$ composition corresponds to a normalized weight of 232.5%; the difference indicates that the synthesized material has some missing-linker defects, corres-

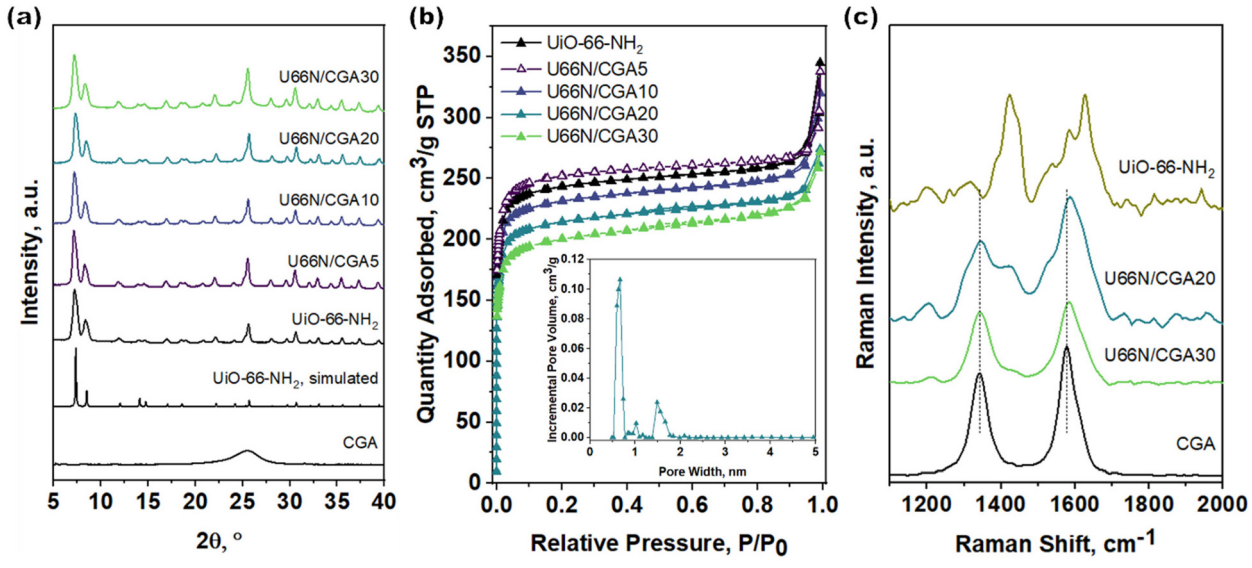


Fig. 2 Structural analysis of U66N/CGA5-30: (a) XRD patterns, with simulated UiO-66-$NH_2$ and CGA included for comparison, (b) $N_2$ adsorption–desorption isotherms, and (c) Raman spectra. The inset in (b) shows the corresponding pore-size distribution for U66N/CGA20. The simulated powder pattern was plotted from the single-crystal structure of UiO-66-$NH_2$ (CCDC 1405751).

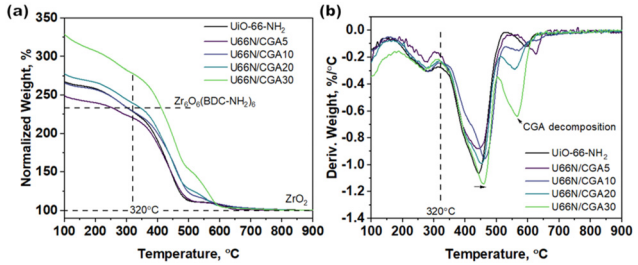


**Fig. 3** (a) TGA and (b) DTA of $scCO_2$-assisted continuous-flow synthesized UiO-66-$NH_2$, and U66N/CGA5-30.

ponding to a defect level of ~0.04 out of 6. At 320 °C, the increase in normalized weight is due to the higher CGA content in U66N/CGA5-30, as CGA retains its mass below 430 °C (Fig. S4). A lower normalized weight of U66N/CGA5 relative to UiO-66-$NH_2$ suggests the missing BDC linkers caused by CGA incorporation. Similarly, the U66N/CGA10 composite shows a normalized mass change to that of UiO-66-$NH_2$, further supporting the formation of defects. The decomposition behaviour of the BDC linkers in U66N/CGA composites is similar to that of UiO-66-$NH_2$, except for a 5 °C shift in the decomposition peak (Fig. 3b).

With respect to material optical properties, incorporation of CGA into UiO-66-$NH_2$ enhances its light absorption in the 350 to 800 nm excitation range. Fig. 4a shows the Kubelka–Munk function, $F(R)$, calculated from diffuse and specular reflection (DSR) measurements. A stronger optical absorption across the visible region is observed with higher CGA content. Tauc analysis[36,37] of the corresponding spectra reveals a systematic decrease in the apparent optical bandgap, from 2.80 eV for pristine UiO-66-$NH_2$ to 2.60, 2.30, and 1.66 eV for the U66N/CGA composites with increasing CGA content (Fig. S9). The reduced apparent bandgap suggests a stronger response of U66N/CGA to lower-energy light excitation.

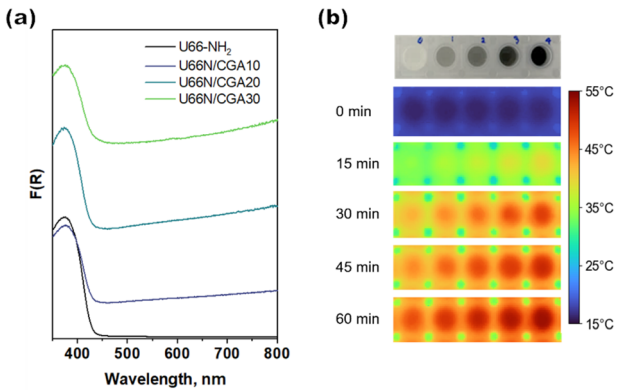


**Fig. 4** (a) DRS-UV-vis spectra of the UiO-66-$NH_2$ and U66N/CGA. (b) Infrared thermal images of UiO-66-$NH_2$ and U66N/CGA aqueous suspensions under simulated solar illumination (0.1 W $cm^{-2}$) during 60 min of testing with 15 min light irradiation intervals. The top row shows the corresponding digital images of the well plate, with CGA content increasing from 0 to 30 wt% from left to right.

Photothermal images show the samples' temperature under continuous light irradiation. The samples were dispersed in water at a concentration of 0.5 mg $mL^{-1}$. The optical photograph (top) shows the appearance of the samples as the CGA content increases. The infrared thermal maps below reveal a composition-dependent increase in temperature. The neat control sample shows minimal heating, whereas samples containing CGA exhibit progressively higher surface temperatures. As the CGA loading increases, the temperature rises systematically, as indicated by the color scale. The U66N/CGA30 dispersion increased from 20 °C to 43 °C within the first 15 min of irradiation and reached a maximum of 55 °C. In practical application, the photothermal effect can accelerate photocatalytic reaction kinetics, as demonstrated in the decomposition of DMNP using UiO-66-$NH_2$/graphene composites.[38]

## Discussion

The synthesis of U66N/CGA in the lab-scale $scCO_2$ continuous flow reactor demonstrates a proof-of-concept for scalable MOF-graphene composite synthesis. HydroGraph Clean Power, Inc. already synthesizes graphene aggregates at scale. For the MOF coating, increased production rates may be achieved by higher precursor throughput and optimizing $CO_2$ flow rates and injection method. Although these optimization strategies may pose engineering challenges, using a larger reactor pressure vessel will allow us to maintain the required residence time and reactant mixing levels. $CO_2$ can be recycled as in current industrial-scale supercritical fluid extraction (SFE) systems. The addition of a product-collection vessel can facilitate *in situ* activation of the MOF/graphene product.[39] A comparison between our synthesis method and other MOF/graphene synthesis methods is detailed in Table S1.

MOF/graphene composites have been studied as photocatalysts in the degradation of dyes and pharmaceuticals.[40–44] UiO-66-$NH_2$ has been reported to catalyze aldol condensates and CWA degradation.[45–47] UiO-66-$NH_2$, as a photocatalyst, may also degrade antibiotics and parabens, while incorporating graphene may enable hydrogen production, $CO_2$ reduction, and improved CWA degradation.[38,48–52] The conformal UiO-66-$NH_2$ shell formed on CGA provides intimate interfacial contact, a feature widely recognized as critical for efficient charge transfer and recombination suppression in hybrid photocatalytic systems.[53,54] Such interface engineering is expected to promote effective coupling between light absorption, charge generation, and surface reaction sites. Defect sites within the UiO-66-$NH_2$ framework may enhance photocatalytic performance by increasing the density of accessible active sites and providing charge-trapping sites that reduce charge recombination.[55–57] In addition, the U66N/CGA component exhibits photothermal heating under light irradiation. Localized photothermal heating has been reported to accelerate surface reaction kinetics by enhancing molecular diffusion and lowering kinetic barriers.[58] Together, these features indi-

cate that the U66N/CGA nanocomposites are a promising platform for photocatalytic applications.

Based on the experimental observations, a mechanistic interpretation of the $scCO_2$-assisted MOF coating process is proposed. The use of $scCO_2$ is critical for achieving a uniform UiO-66-$NH_2$ coating. Although the CGA is functionalized with carboxyl groups, this surface functionalization alone is insufficient to promote conformal MOF growth on the CGA surface. This is evidenced by control solvothermal syntheses conducted under otherwise identical conditions, which indicates no observable heterogeneous nucleation of UiO-66-$NH_2$ on CGA. Despite limited reports on MOF coatings, synthesis in $scCO_2$ may offer advantages for coating metal oxides and polymers onto carbon nanotubes.[59] The role of $scCO_2$ is generally attributed to several key aspects: (i) the solubility of reactants can be tuned by adjusting the density of the supercritical fluid, thereby shifting reaction equilibria; (ii) rapid mass and heat transfer in $scCO_2$ reduces the diffusion limited steps and accelerates global reaction kinetics; (iii) reduced interfacial tension at the solid–liquid interface in the presence of $scCO_2$ improves wetting of the substrate surface;[60] and (iv) the near-zero surface tension of $scCO_2$ enables solvent removal without capillary stresses, thereby preserving the structural integrity of coated surfaces. This work suggests that the reduced effective dielectric constant of the solvent mixture enhances the adsorption of $Zr^{4+}$ species onto the CGA surface, thereby providing a high density of nucleation sites for subsequent MOF growth. The diffusion of Zr-MOF precursors and the fast kinetics of non-classical crystal growth also play essential roles in the formation of MOF shells. Future investigation should consider elucidating MOF synthesis and surface coating mechanisms and include the analysis of elemental oxidation states.

## Conclusions

In this work, we demonstrated a scalable, $scCO_2$-assisted continuous-flow approach for the synthesis of UiO-66-$NH_2$/CGA nanocomposites with well-controlled interfacial architecture. By integrating chamber-explosion-derived layered graphene-based CGA with $scCO_2$-assisted MOF synthesis, this method overcomes key limitations of conventional batch and solvothermal approaches, such as long reaction times, poor interfacial contact, and limited throughput. The $scCO_2$ environment plays a critical role in promoting rapid nucleation and conformal growth of UiO-66-$NH_2$, resulting in uniform MOF shells coating fractal CGA clusters within 1.2 min and at several grams per hour yields. The U66N/CGA nanocomposites maintain crystallinity, high BET surface areas, and pore structures of the parent MOF. Thermal and spectroscopic analyses indicate that CGA incorporation induces defect formation without compromising the structural integrity of UiO-66-$NH_2$ or inducing significant chemical modification of the graphene phase. Increasing CGA content yields a strong photothermal response under simulated solar illumination, confirming efficient photothermal conversion. The resulting UiO-66-$NH_2$/CGA materials show strong potential for photocatalytic and related energy and environmental applications. Current research focuses on understanding the mechanism of $scCO_2$-assisted coating and extending this approach to a broader range of MOFs and nanoscale substrates.

## Author contributions

Almond Lau: writing – original draft, writing – review & editing, methodology, investigation, formal analysis, conceptualization. Ji Feng: writing – original draft, writing – review & editing, visualization, validation, methodology, investigation, formal analysis, conceptualization. Stefan Bossmann: design of graphene substrate, writing – review & editing, resources. Dymphna Sebastian: design and synthesis of reactive graphene substrate. Christopher M. Sorensen: writing – review & editing, resources. Igor V. Novosselov: writing – review & editing, supervision, project administration, methodology, conceptualization.

## Conflicts of interest

There are no conflicts to declare.

## Data availability

The data supporting this article have been included as part of the supplementary information (SI). Supplementary information: materials, process diagram of the $scCO_2$ continuous flow reactor setup, structural and morphological characterization of CGA and U66N/CGA composites. See DOI: https://doi.org/10.1039/d6nr00739b.

## Acknowledgements

This work was funded by the Defense Threat Reduction Agency (DTRA) under the grants HDTRA12410010 and HDTRA12610005. Part of this work was conducted at the Molecular Analysis Facility, a National Nanotechnology Coordinated Infrastructure (NNCI) site at the University of Washington with partial support from the National Science Foundation *via* awards NNCI-1542101 and NNCI-2025489. Material characterization was partly conducted at the Clean Energy Institute.

## References

1 J. Xu, S. He, H. Zhang, J. Huang, H. Lin, X. Wang and J. Long, *J. Mater. Chem. A*, 2015, **3**, 24261–24271.
2 K. Jayaramulu, S. Mukherjee, D. M. Morales, D. P. Dubal, A. K. Nanjundan, A. Schneemann, J. Masa, S. Kment,

 

W. Schuhmann, M. Otyepka, R. Zbořil and R. A. Fischer, *Chem. Rev.*, 2022, **122**, 17241–17338.
3 K. Wang, K. N. Hui, K. S. Hui, S. Peng and Y. Xu, *Chem. Sci.*, 2021, **12**, 5737–5766.
4 C. Chen, L. Fei, B. Wang, J. Xu, B. Li, L. Shen and H. Lin, *Small*, 2024, **20**, 2305066.
5 A. Chatterjee, L. Wang and P. Van Der Voort, *Chem. Commun.*, 2023, **59**, 3627–3654.
6 Y. Shen, A. Tissot and C. Serre, *Chem. Sci.*, 2022, **13**, 13978–14007.
7 K. Jayaramulu, M. Horn, A. Schneemann, H. Saini, A. Bakandritsos, V. Ranc, M. Petr, V. Stavila, C. Narayana, B. Scheibe, Š. Kment, M. Otyepka, N. Motta, D. Dubal, R. Zbořil and R. A. Fischer, *Adv. Mater.*, 2021, **33**, 2004560.
8 J. Aguila-Rosas, F. J. Cano, A. Nagaya, C. T. Quirino-Barreda, M. De Jesús Martínez Ortiz, A. G. Vargas, I. A. Ibarra and E. Lima, *Chem. Commun.*, 2025, **61**, 11706–11731.
9 Q. Zhao, Y. Li, W. Jia and B. Li, *Chem. Commun.*, 2026, **62**, 1015–1030.
10 R. Kumar, K. Jayaramulu, T. K. Maji and C. N. R. Rao, *Chem. Commun.*, 2013, **49**, 4947.
11 M. Jahan, Q. Bao, J.-X. Yang and K. P. Loh, *J. Am. Chem. Soc.*, 2010, **132**, 14487–14495.
12 A. U. Rehman, S. Ullah, N. A. Khan, M. S. Javed, L. Gurbanova, M. A. Ismail, A. Mohammad, S. S. A. Shah and M. A. Nazir, *Chem. – Asian J.*, 2025, **20**, e00453.
13 H. Qu, L. Huang, Z. Han, Y. Wang, Z. Zhang, Y. Wang, Q. Chang, N. Wei, M. J. Kipper and J. Tang, *J. Porous Mater.*, 2021, **28**, 1837–1865.
14 X. Liu, T. Sun, J. Hu and S. Wang, *J. Mater. Chem. A*, 2016, **4**, 3584–3616.
15 D. Bigdelifam and M. Hashemi, *ACS Omega*, 2025, **10**, 16184–16193.
16 P. Jagódka, K. Matus and A. Łamacz, *Molecules*, 2022, **27**, 7082.
17 Z. Bian, J. Xu, S. Zhang, X. Zhu, H. Liu and J. Hu, *Langmuir*, 2015, **31**, 7410–7417.
18 S. L. Griffin, M. L. Briuglia, J. H. Ter Horst and R. S. Forgan, *Chem. – Eur. J.*, 2020, **26**, 6910–6918.
19 X. Sang, J. Zhang, J. Xiang, J. Cui, L. Zheng, J. Zhang, Z. Wu, Z. Li, G. Mo, Y. Xu, J. Song, C. Liu, X. Tan, T. Luo, B. Zhang and B. Han, *Nat. Commun.*, 2017, **8**, 175.
20 M. A. Artsiusheuski, N. P. M. Casati, A. H. Clark, M. Nachtegaal, R. Verel, J. A. Van Bokhoven and V. L. Sushkevich, *Angew. Chem., Int. Ed.*, 2025, **64**, e202415919.
21 K. A. Adegoke and P. F. Tseki, *Carbon Capture Sci. Technol.*, 2025, **17**, 100523.
22 M. J. Dzinnik, N. E. Akmaz, A. Hannebauer, A. Schaate, P. Behrens and R. J. Haug, *Commun. Mater.*, 2024, **5**, 38.
23 K. Jayaramulu, M. E. Dmello, K. Kesavan, A. Schneemann, M. Otyepka, S. Kment, C. Narayana, S. B. Kalidindi, R. S. Varma, R. Zboril and R. A. Fischer, *J. Mater. Chem. A*, 2021, **9**, 17434–17441.
24 Y. Liang, H. Wang, H. S. Casalongue, Z. Chen and H. Dai, *Nano Res.*, 2010, **3**, 701–705.
25 A. Nepal, G. P. Singh, B. N. Flanders and C. M. Sorensen, *Nanotechnology*, 2013, **24**, 245602.
26 J. P. Wright, S. Sigdel, S. Corkill, J. Covarrubias, L. Leban, A. Nepal, J. Li, R. Divigalpitiya, S. H. Bossmann and C. M. Sorensen, *Nano Sel.*, 2022, **3**, 1054–1068.
27 S. Sigdel, J. P. Wright, J. Covarrubias, A. Sekar, K. Mutthukumar, S. H. Bossmann, J. Li, A. Nepal, S. Corkill and C. M. Sorensen, *Carbon Trends*, 2023, **13**, 100306.
28 C. Sorensen, A. Nepal and G. P. Singh, *US Pat*, US9440857, 2016.
29 E. G. Rasmussen, J. Kramlich and I. V. Novosselov, *ACS Sustainable Chem. Eng.*, 2020, **8**, 9680–9689.
30 E. G. Rasmussen, J. Kramlich and I. V. Novosselov, *Chem. Eng. J.*, 2022, **450**, 138053.
31 J. Feng, A. Lau and I. V. Novosselov, *Nanoscale*, 2024, **16**, 22142–22151.
32 C. M. Sorensen, S. Sigdel, C. Bartlam, S. H. Bossmann, K. Breure, S. Corkill, R. Divigalpitiya, A. Ejas, T. Eldridge, R. Estes, S. Li and A. Shakil, *Graphene 2D Mater.*, 2025, **10**, 43–56.
33 Y. Wang, X. Zhou, Y. Jin, X. Zhang, Z. Zhang, Y. Wang, J. Liu, M. Wang, Y. Xia, P. Zhao, Z. Zhang and H. Wang, *Phys. Rev. B*, 2019, **100**, 241407.
34 J. E. Lee, G. Ahn, J. Shim, Y. S. Lee and S. Ryu, *Nat. Commun.*, 2012, **3**, 1024.
35 A. Das, S. Pisana, B. Chakraborty, S. Piscanec, S. K. Saha, U. V. Waghmare, K. S. Novoselov, H. R. Krishnamurthy, A. K. Geim, A. C. Ferrari and A. K. Sood, *Nat. Nanotechnol.*, 2008, **3**, 210–215.
36 J. Zhang, Y. Hu, J. Qin, Z. Yang and M. Fu, *Chem. Eng. J.*, 2020, **385**, 123814.
37 W. Hou, C. Chen, D. Xie and Y. Xu, *ACS Appl. Mater. Interfaces*, 2023, **15**, 2911–2921.
38 L. Song, T. Zhao, D. Yang, X. Wang, X. Hao, Y. Liu, S. Zhang and Z.-Z. Yu, *J. Hazard. Mater.*, 2020, **393**, 122332.
39 Ž. Knez, E. Markočič, M. Leitgeb, M. Primožič, M. Knez Hrnčič and M. Škerget, *Energy*, 2014, **77**, 235–243.
40 Q. V. Thi, M. S. Tamboli, Q. Thanh Hoai Ta, G. B. Kolekar and D. Sohn, *Mater. Sci. Eng., B*, 2020, **261**, 114678.
41 L. Huang and B. Liu, *RSC Adv.*, 2016, **6**, 17873–17879.
42 Y. Wan, J. Wang, F. Huang, Y. Xue, N. Cai, J. Liu, W. Chen and F. Yu, *RSC Adv.*, 2018, **8**, 34552–34559.
43 Z. Wu, Z. Chen, J. Chen, X. Ning, P. Chen, H. Jiang and H. Qiu, *Environ. Sci.: Nano*, 2022, **9**, 4609–4618.
44 C. Yang, X. You, J. Cheng, H. Zheng and Y. Chen, *Appl. Catal., B*, 2017, **200**, 673–680.
45 J. Hajek, M. Vandichel, B. Van De Voorde, B. Bueken, D. De Vos, M. Waroquier and V. Van Speybroeck, *J. Catal.*, 2015, **331**, 1–12.
46 D. T. Lee, J. Zhao, G. W. Peterson and G. N. Parsons, *Chem. Mater.*, 2017, **29**, 4894–4903.
47 G. W. Peterson, M. R. Destefano, S. J. Garibay, A. Ploskonka, M. Mcentee, M. Hall, C. J. Karwacki,

J. T. Hupp and O. K. Farha, *Chem. – Eur. J.*, 2017, **23**, 15913–15916.
48 Y. L. Wang, A. Gómez-Avilés, S. Zhang, J. J. Rodriguez, J. Bedia and C. Belver, *J. Environ. Chem. Eng.*, 2023, **11**, 109744.
49 R. R. Solís, M. Peñas-Garzón, C. Belver, J. J. Rodriguez and J. Bedia, *J. Environ. Chem. Eng.*, 2022, **10**, 107122.
50 M. Peñas-Garzón, M. J. Sampaio, Y. L. Wang, J. Bedia, J. J. Rodriguez, C. Belver, C. G. Silva and J. L. Faria, *Sep. Purif. Technol.*, 2022, **286**, 120467.
51 Y. Wang, Y. Yu, R. Li, H. Liu, W. Zhang, L. Ling, W. Duan and B. Liu, *J. Mater. Chem. A*, 2017, **5**, 20136–20140.
52 X. Wang, X. Zhao, D. Zhang, G. Li and H. Li, *Appl. Catal., B*, 2018, **228**, 47–53.
53 X. Li, J. Yu, S. Wageh, A. A. Al-Ghamdi and J. Xie, *Small*, 2016, **12**, 6640–6696.
54 Q. Huang, S. Tian, D. Zeng, X. Wang, W. Song, Y. Li, W. Xiao and C. Xie, *ACS Catal.*, 2013, **3**, 1477–1485.
55 Y. He, C. Li, X.-B. Chen, Z. Shi and S. Feng, *ACS Appl. Mater. Interfaces*, 2022, **14**, 28977–28984.
56 A. De Vos, K. Hendrickx, P. Van Der Voort, V. Van Speybroeck and K. Lejaeghere, *Chem. Mater.*, 2017, **29**, 3006–3019.
57 C. Zhou, B. Yuan, S. Zhang, G. Yang, L. Lu, H. Li and C. Tao, *ACS Appl. Mater. Interfaces*, 2022, **14**, 23383–23391.
58 I. S. Khan, L. Garzon-Tovar, D. Mateo and J. Gascon, *Eur. J. Inorg. Chem.*, 2022, **2022**, e202200316.
59 R. Sui and P. Charpentier, *Chem. Rev.*, 2012, **112**, 3057–3082.
60 Z. Sun, X. Zhang, N. Na, Z. Liu, B. Han and G. An, *J. Phys. Chem. B*, 2006, **110**, 13410–13414.